RESEARCH ARTICLE

ADVANCED
INTELLIGENT
SYSTEMS
Open Access

www.advintellsyst.com

Robust Lead-Free Perovskite Nanowire Array-Based Artificial Synapses Exemplifying Gestalt Principle of Closure via a Letter Recognition Scheme

Swapnadeep Poddar, Zhesi Chen, Zichao Ma, Yuting Zhang, Chak Lam Jonathan Chan, Beitao Ren, Qianpeng Zhang, Daquan Zhang, Guozhen Shen, Haibo Zeng, and Zhiyong Fan*

Dedicated to the memory of Late Prof. Indrani Mukherjee, Department of Applied Psychology, University of Calcutta, India.

The Gestalt principles of perceptual learning elucidate how the human brain categorizes and comprehends a set of visual elements grouped together. One of the principles of Gestalt perceptual learning is the law of closure which propounds that human perception has the proclivity to visualize a fragmented object as a preknown whole by bridging the missing gaps. Herein, a letter recognition scheme emulating the Gestalt closure principle is demonstrated, utilizing artificial synapses made of 3D integrated $MA_3Bi_2I_9$ (MBI) perovskite nanowire (NW) array. The artificial synapses exhibit short-term plasticity (STP) and long-term potentiation (LTP) and a transition from STP to LTP with increasing number of input electrical pulses. Initiatory ab initio molecular dynamics (AIMD) simulations attribute the conductance change in the MBI NW artificial synapses to the rotation of MA^+ clusters, culminating in charge exchange between MA^+ and $Bi_2I_9^{3-}$. Each device yields 40 conductance states with excellent retention $>10^5$ s, minimal variation (2σ/mean) $<10\%$, and endurance of $\approx 10^5$ cycles. MBI NW-based artificial neural network (ANN) is constructed to recognize fragmented letters alike their distinction in unabridged form and also the gradual withering of synaptic connectivity with engendered missing fragments is demonstrated, thereby successfully implementing Gestalt closure principle.

1. Introduction

In the earlier half of the 20th century, scientists Wertheimer, Köhler, and Kofka postulated the principles of Gestalt learning based on the premise that human perception is not always the same as a simple amalgam of input sensory stimuli. In other words, the whole of what we sometimes visually perceive is different from the sum of its parts[1–3] Gestalt laws of perception have been categorized as principles of similarity, connection, proximity, symmetry, continuity, and closure. The principle of closure states that humans tend to systemize their perception into complete objects that are known to them beforehand by bridging the existing gaps in input stimuli.[4] Owing to the complexity of the human brain and its associated thought processes, it is extremely challenging for researchers to decipher the origin of these perceptual habits or to emulate them effectively using artificial systems. Of late, with the inception of neuromorphic computing,

S. Poddar, Z. Chen, Z. Ma, Y. Zhang, C. L. J. Chan, B. Ren, Q. Zhang, D. Zhang, Z. Fan
Department of Electronic & Computer Engineering
The Hong Kong University of Science and Technology
Clear Water Bay, Kowloon, Hong Kong SAR, China
E-mail: eezfan@ust.hk

Ⓘ The ORCID identification number(s) for the author(s) of this article can be found under https://doi.org/10.1002/aisy.202200065.

G. Shen
State Key Laboratory for Superlattices and Microstructures
Institute of Semiconductors
Chinese Academy of Sciences & Center of Materials Science and Optoelectronic Engineering
University of Chinese Academy of Sciences
Beijing 100083, China

H. Zeng
MIIT Key Laboratory of Advanced Display Materials and Devices
Institute of Optoelectronics & Nanomaterials
School of Materials Science and Engineering
Nanjing University of Science and Technology
Nanjing 210094, China

scientists have successfully emulated brain activities like facial classification, image processing, etc. at the hardware and device level with artificial neural networks (ANNs).[5,6] As evident from past literature, ANNs have the capability to mimic a variety of human perceptual and cognitive traits utilizing the inherent similarity between neuron-synaptic interconnects in artificial and biological synapses.[7–11] At the device level, neuromorphic chips mostly comprise assembled memristors that behave as artificial synapses, performing the processing tasks akin to the human brain. Besides traditional switching layers in resistive RAM (RRAM)-based memristors, halide perovskite materials that have carved a niche for themselves in the genre of optoelectronics are now also finding their way in RRAM-based neuromorphic hardware.[12,13] Plethora of charge and ion movement pathways, excellent hysteresis, high response to optical stimuli, and presence of defect states modulating the conductivity are reasons why halide perovskite materials are emerging as promising candidates for RRAMs in neuromorphic devices. However, previously reported studies on halide perovskite-based neuromorphic systems demonstrate simple short-term plasticity and long-term potentiation (STP and LTP) learning rules and no sophisticated processing tasks at the device level have been demonstrated.[14] Specifically, being extremely sensitive to environmental conditions and dearth of protection mechanism to instill material and electrical stability in thin-film (TF)-based active layers, the performance metrics of halide perovskite in terms of achieving state-of-the-art standard for neuromorphic applications, have not been achieved yet. The material and electrical instability impedes the accessing of temporally stable and robust LTP conduction states, which in turn thwarts the performing of neural network-based processing in halide perovskite devices.

In this work, we developed artificial synapses comprising methyl ammonium bismuth iodide (MA$_3$Bi2I$_9$ or MBI) perovskite nanowires (NWs) sandwiched between indium-doped tin oxide (ITO) and aluminum (Al) electrodes. The MBI NWs were embedded in a nanoengineered porous alumina membrane (PAM) which imparted excellent material and electrical stability to the perovskite, thereby improving the synaptic and neuromorphic device performance.[15–18] Using MBI as the perovskite active layer also helped in eluding the toxicity issue associated with lead halide perovskite.[19] Apart from the electrical and material stability-related advantages over traditional halide perovskite TF-based devices, the distinct advantages of the vertical NWs in PAM over previously reported other material-based NW artificial synapses must be mentioned here. Previous reports have explored the utilization of single horizontal nanowires for building artificial synapses that suffer from the absence of large-scale assembly of NWs hindering the realization of physical ANNs, a problem that can be effectively navigated with ultrahigh-density ($\approx 10^{10}$ cm^{-2}) vertically assembled MBI NWs.[20,21] Horizontal and vertical arrays of NWs have been utilized previously for developing synaptic transistors and two-terminal artificial synapses.[22,23] However they lack protection mechanism in the form of PAM walls and controllable assembly techniques to grow ultrahigh density ordered wire array. These inhibit the utilization of such methods for environmentally delicate materials like halide perovskite as well as debilitate the temporal stability and robustness of the LTP conduction states, thereby thwarting the implementation of such synaptic devices in large-scale physical ANNs

for complex neuromorphic processing tasks. Furthermore, the NWs in the PAM are electrically isolated from one another, which suppresses lateral electrical leakages, and the supremely high density of NWs paves the way for large-scale ANNs with scaled-down synaptic device sizes.

The MBI NW devices exhibited STP behavior by responding to input sensory electrical pulses of varying amplitude, duration, and interval. A gradual transition from the STP–to-LTP mode was observed with increased number of stimulating pulses and consequently the devices demonstrated LTP behavior by responding to rate as well as the number of incoming LTP pulses and the pre-/postsynaptic delay between pulses. For the monocrystalline MBI NWs, the origin of the conductivity change was traced with the aid of first principle ab initio molecular dynamics simulations. It was deciphered that the rotation of the MA$^+$ clusters in the MBI crystal structure causes charge transfer between MA$^+$ and Bi$_2$I$_9$$^{3-}$, resulting in the plasticity or gradual conductivity change. At least 40 accessible conductance states were obtained by applying input LTP pulse trains. The conductance states could be retained $>10^5$ s and they showed minimal jitter with variation (2σ where 'σ' is the standard deviation/mean) $<10\%$ and endurance $\approx 10^5$ cycles. A single-layered ANN, built with MBI NW devices as the unit blocks, was trained with synaptic weights obtained from delta rule-based simulations. A letter recognition scheme was developed such that the ANN could successfully discriminate between fragmented letters 'H,K,U,S,T' alike nonfragmented ones. Also via the MBI NW-based ANN, it was experimentally demonstrated that with more missing pieces of a single letter, the distinguishing ability and subsequent synaptic connectivity of the MBI NW artificial synapses wither, much like our perceptual habit. The successful implementation of this letter recognition scheme emulating Gestalt closure principle with MBI NWs-based ANN here can propel neuromorphic hardware to perform pattern recognition tasks emulating human cognition as well as elevate halide perovskites to the state-of-the-art standard in performing neuromorphic processing tasks.

2. Results and Discussion

2.1. Concept and Morphological Study

Figure 1a demonstrates the logical corroboration between Gestalt closure principle in human brain and letter recognition-based Gestalt closure in the artificial synaptic array based on MBI NWs. The top row shows how the human brain perceives an incomplete and fragmented image of a butterfly but still is able to organize the image as that of a complete butterfly. Similarly the bottom row of Figure 1a shows the device structure of the artificial synaptic NW array. MBI perovskite NWs are rooted in the insulating PAM template with ITO and Al as top and bottom electrodes, respectively. The input stimuli to the device are a set of defected letters 'H,K,U,S,T' and the output shows the complete version of the letters 'H,K,U,S,T' once the MBI NW device has successfully completed the recognition task emulating the Gestalt learning of closure. Figure 1b shows the transmission electron microscopy (TEM) image of the MBI NW array surrounded by the aluminum oxide (Al$_2$O$_3$) walls. The diameter of an individual NW is ≈ 40 nm, grown by a vapor–solid–solid
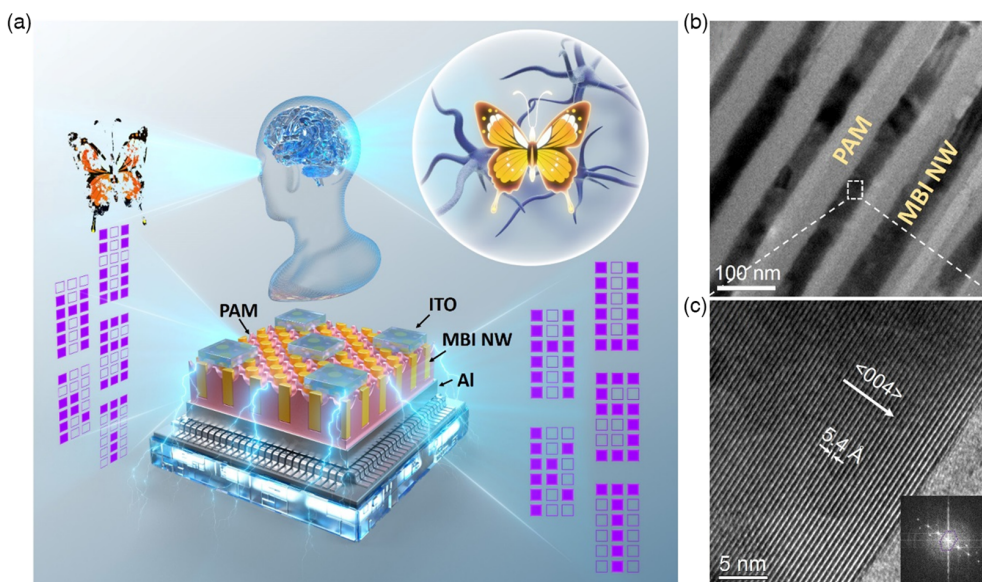
Figure 1. Concept and morphological study. a) Top: The organization of a fragmented image of a butterfly into a complete one, as performed by the human brain, thereby exhibiting implementation of Gestalt principle of closure. Bottom: Fragmented letters H, K, U, S, and T being perceived as complete letters post implementation of letter recognition in artificial MBI NW synaptic array-based neuromorphic device. The MBI NWs, rooted in the PAM, are clubbed between ITO and Al electrical contacts. b) TEM image of MBI NWs in the PAM. Diameters of the NWs are around ≈40 nm. The lamella was prepared by a low-energy focused ion beam cut (for details see Experimental Section). c) HRTEM of a single-crystalline MBI NW with a lattice spacing of 5.4 Å, corresponding to the array shown in (b). Inset shows the FFT reciprocal hexagonal lattice (shaded in purple) of MBI NW.

reaction (VSSR) (see Experimental Section). The energy-dispersive X-Ray spectroscopy (EDS) mapping corresponding to the MBI NW array is shown in Figure S1, Supporting Information. The high-resolution transmission electron microscopy (HRTEM) image of an individual MBI NW is shown in Figure 1c, which exhibits excellent single crystallinity and a lattice spacing of 5.4 Å corresponding to the [004] plane.[24–26] Figure S2, Supporting Information, shows the X-Ray diffraction (XRD) and photoluminescence (PL) spectra of the MBI NWs in PAM, conforming with the previously reported MBI material characterizations.[26] The inset shows the fast Fourier transform (FFT) reciprocal lattice of the MBI NW, exhibiting the typical hexagonal lattice structure of MBI perovskite.[27]

2.2. Artificial Synaptic Characteristics

Synaptic plasticity refers to the modulation of the strength of neuronal connections in the brain that is directly related to behavioral modifications, learning, and memory. Plasticity can be broadly of types: STP which results in short-term habituation and transient changes in response to external stimuli and long-term potentiation (LTP) that results in prolonged modification synaptic strength.[28] The MBI NW artificial synapses exhibited STP behavior in the form of synaptic voltage-dependent plasticity (SVDP), synaptic duration-dependent plasticity (SDDP), and paired pulse facilitation (PPF), as shown in **Figure 2**a–c. Figure S3, Supporting Information, details out the various amplitude, duration, and interval schemes used for the input SVDP, SDDP, and PPF electrical pulses. As shown in Figure 2d, with a gradual increase in the number of input presynaptic pulses from

2 to 50, the synaptic connectivity in terms of durability and conductance is strengthened. With 2 pulses of 5 V amplitude and reading with 0.1 V, the postsynaptic current of ≈0.1 mA could only be retained for 400 ms (inset of Figure 2d). However with 50 such input pulses, the postsynaptic current of ≈10 mA could be retained without any degradation for 20 s, indicating a transformation from STP to LTP. Corresponding to Figure 2d, the synaptic number-dependent plasticity (SNDP) has been demonstrated in Figure 2e, which shows the increase in device conductance with increasing number of input pulses. In the LTP mode, the MBI NW devices also demonstrated synaptic rate-dependent plasticity (SRDP) when a train of 20 input pulses of 10 ms width and 5 V amplitude preceded and succeeded by reading voltage pulse of 0.1 V height was fed to the devices, such that the intervals between the pulses in the train were varied from 2 to 50 ms (see Figure 2f and supporting information Figure S4a–c, Supporting Information). A gradual diminishing of the conductance change (ΔG) was observed with increasing pulse interval, mimicking biological synapses.[29] As shown in Figure 2g and S4d–f, Supporting Information, the MBI NW devices also showed spike-time-dependent plasticity (STDP). The device conductance change (ΔG) was modulated by the delay between pre and postsynaptic pulses. Figure 2h shows the potentiation–depression characteristics of the MBI NW devices for 40 input pulses. A gradual change in device conductance was observed indicating the accumulation effect.[30] 5 V/10 ms for potentiation, −5 V/10 ms for depression, and read pulse 0.1 V/10 ms were used for the potentiation–depression measurement. The device-to-device variation data as shown in Figure 2a,b,h are obtained from 15 NW artificial synapses on different PAM chips.
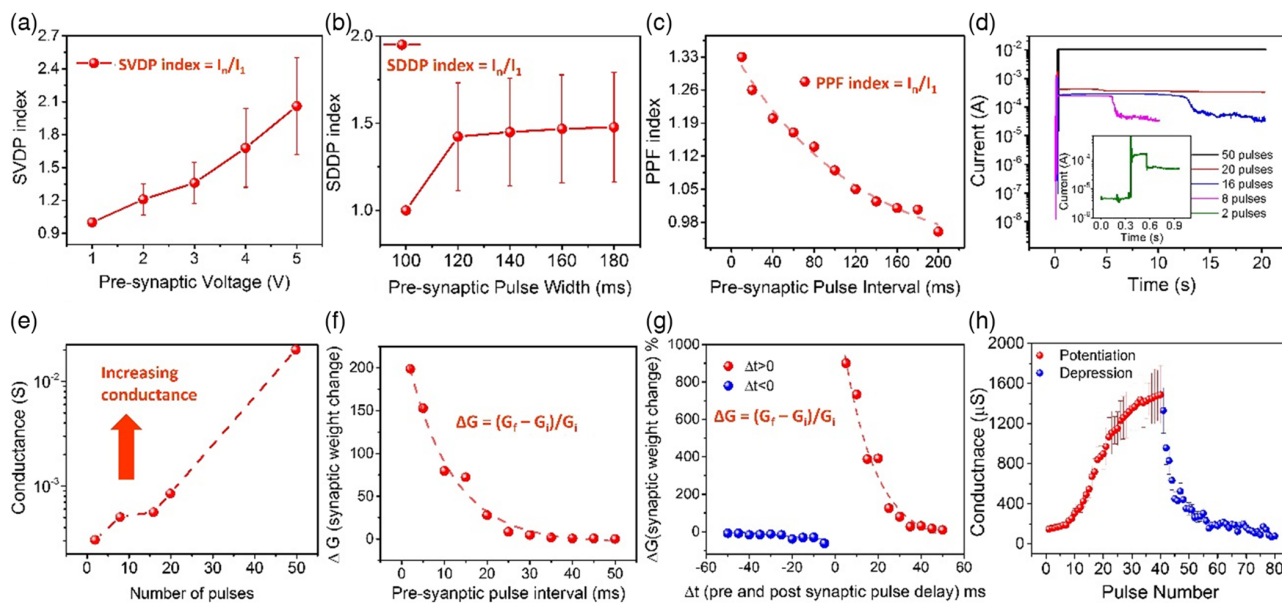
Figure 2. Synaptic characteristics of MBI NW device. a) Synaptic voltage-dependent plasticity demonstrated by the MBI NW device. The interval and width of the input pulses were fixed at 50 and 10 ms respectively. b) Synaptic duration-dependent plasticity demonstrated by the MBI NW device. The amplitude and interval of the input pulses were fixed at 5 V and 100 ms respectively. c) Paired pulse facilitation demonstrated by the MBI NW device. The amplitude and duration of the input pulses were fixed at 5 V and 100 ms, respectively. d) STP-to-LTP transformation demonstrated by the MBI NW device, with increasing number of input pulses. The amplitude, width, and interval of the pulses were fixed at 5 V, 10 ms, and 10 ms, respectively. e) Synaptic number-dependent plasticity demonstrated by the MBI NW device, corresponding to (d). f) Spike-rate-dependent plasticity demonstrated by the MBI NW device. The pulse amplitude, number, width, and interval were fixed at 5 V, 20, 10 ms, and 10 ms respectively. g) Spike-time-dependent plasticity demonstrated by the MBI NW device. The width and voltage of the pulses were fixed at 50 ms and 5 V, respectively. h) Potentiation-depression characteristics of MBI NW device. The amplitude and width of the pulses were fixed at 5 V/10 ms and −5 V/10 ms for the potentiation and depression, respectively. A reading pulse of 0.1 V and 10 ms width were used to read out the conductance.

As shown in Figure S5, Supporting Information, the device-to-device variability of the performance parameters can be reduced by ≈3 times if the devices are on the same PAM chip due to better material homogeneity ascribed to relatively more uniform electrodeposition of precursor Bi metal. The device varaibility can be improved further with solution-processed polycrytalline NWs with better material uniformity among different PAM chips.
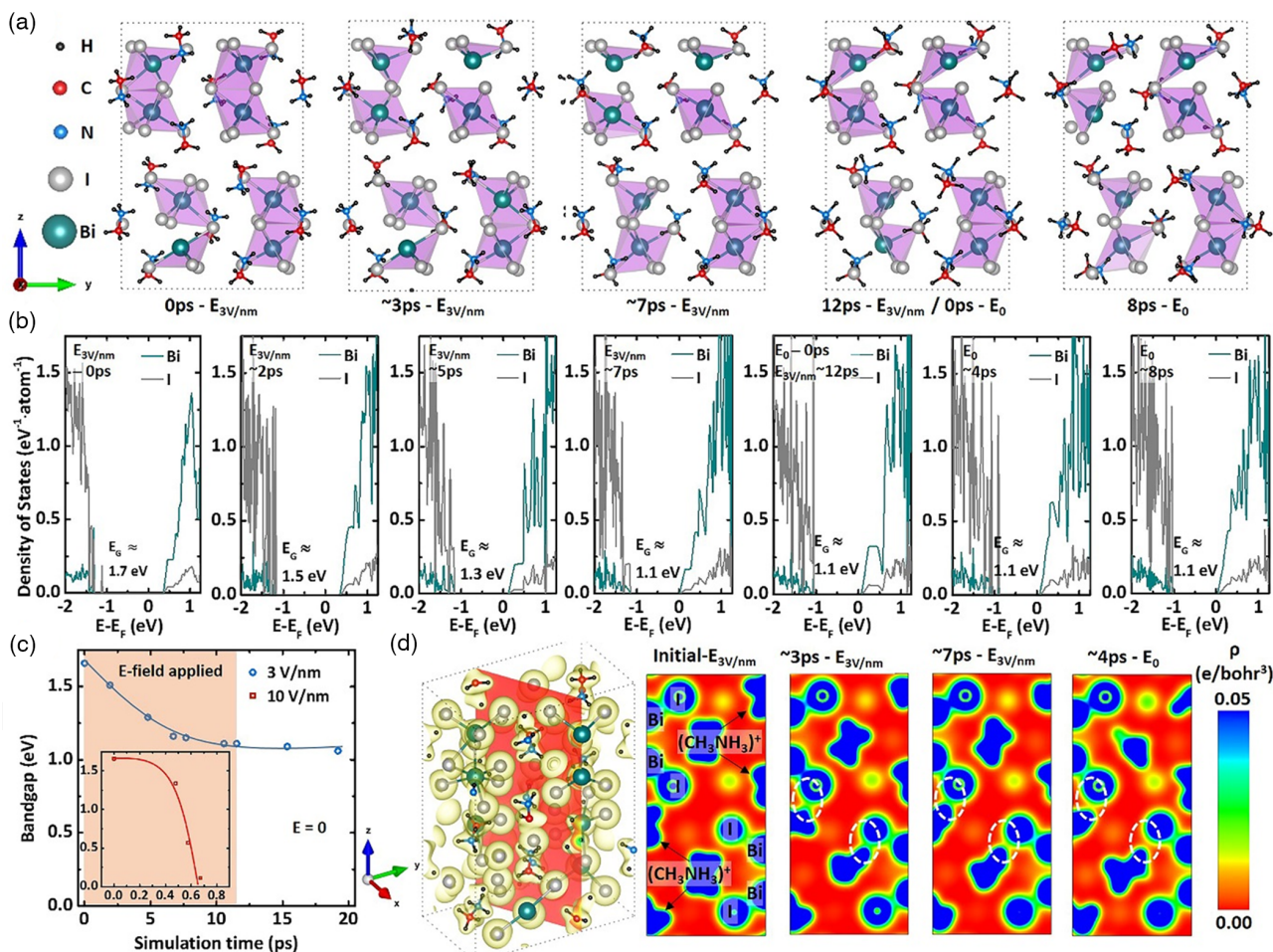
2.3. Molecular Dynamics Simulation to Decipher the Conductance Modulation in Monocrystalline MBI

The origin of plasticity or conductance change in polycrystalline metal halide perovskite-based artificial synapses or memory devices with inert electrodes has been traditionally ascribed to the halide ion-mediated charge trapping and detrapping in the defect states, attributing these devices to the valence change mechanism (VCM) genre.[31] However, as seen in Figure 1c, the MBI perovskite NWs are predominantly single crystalline and the presence of such defect states must be minimal.[27] On the other hand, the ionized halogen atoms trigger redox reactions and form gaseous products and eventually decompose the perovskite lattice structure.[32,33] Especially when there is a bias voltage and current to provide reaction energy, in this case, once iodine vacancies are formed, the avalanche effect may cause rapid decomposition of the MBI lattice structure. However, as will be later discussed, monocrystalline MBI NW devices showed

excellent LTP retention of 10^5 s under electrical bias without any degradation as compared with the polycrystalline TF counterpart which produced brittle LTP states that could last for ≈3.7×10^4 s. Therefore the possibility of forming iodide vacancies in the MBI NW devices is minuscule. Hence to decipher the origin of gradual conductance modulation in monocrystalline MBI perovskite, we carried out ab initio-based molecular dynamics (AIMD) simulations and observed the evolution of the primitive cell structure under electric field and a plausible alternate conduction modulation mechanism is hereby proposed.

The simulation was performed with 2 periods. To investigate the conductance modulation mechanism, the simulation starts with a relaxed primitive cell structure of MBI and electric field of 3 V nm^{-1} ($E_{3V\,nm^{-1}}$) was applied along the z-axis to bring the atomic structure to a new equilibrium. After that, a relaxation simulation without electric field (E_0) was performed to study the stability of the structure. A video recording the AIMD simulation has been provided in Movie S1, Supporting Information.

The primitive cell structures of MBI obtained from the AIMD simulation are plotted in **Figure 3**a. The initial relaxed atomic structure of MBI shows the trigonal lattice symmetry of the bonded bismuth (Bi) atoms and the iodine (I) atoms; $CH_3NH_3^+$ (MA$^+$) molecules fill in the spaces between the adjacent trigonal lattice of $Bi_2I_9^{3-}$, confirming the high crystallinity of the material. In comparison, the evolution of phase structure in

Figure 3. Molecular dynamics simulation to decipher the conductance modulation in monocrystalline MBI. a) Evolution of the atomic structure of MBI perovskite. The sample primitive cell structures obtained at the beginning, the end, and in the middle of the molecular dynamic simulation are plotted. The result shows that the Bi—I-bonded framework has been largely preserved despite that the original trigonal phase is a bit twisted in the MD simulation with electric field. The MA$^+$ clusters, in contrast, are forced to rotate under electric field, and reach a new stable position in electric field. b) Atom-PDoS of the MBI structure obtained in MD simulation. The combined effect of material phase deformation and the rotation of MA$^+$ clusters result in a reduced bandgap and increased electron doping of MBI. c) Evolution of the bandgap of MBI under electric field of 3 and 10 V nm^{-1}. d) Electron charge density distribution of MBI. The 3D illustration in a primitive cell shows the isosurface of electron density of 0.05 e bohr^{-3}, and the 2D plots of electron density are sliced from the 3D data using the lattice plane shown in red. As highlighted by the white circles, strong electron exchange is observed when the MA$^+$ clusters rotate under electric field, whereas the interaction drops off when the MA$^+$ clusters have reached the new stable state. Hence, the electron interaction is plausibly the origin of doping and PDoS changes.

MBI under electric field is reflected by the slight distortion of the trigonal symmetry of $Bi_2I_9^{3-}$ and the rotation of MA$^+$. Particularly, the progress of structure evolution of MBI can be observed by the rotating MA$^+$ clusters. In this simulation, the MA$^+$ clusters show drastic changes in position and orientation during the first 7 ps, while it settles to a position during the rest of the simulation, which indicates that the electric field drives the structure of MBI to evolve and reach an alternative equilibrium.

To bolster the postulate, the atom-projected density of states (PDoS) of the primitive cell structures is plotted in Figure 3b. In the MBI material, most of the DoS is contributed by the Bi atoms and I atoms (see Figure S6, Supporting Information); as such, the PDoS analysis of hydrogen, carbon, and nitrogen atoms is omitted. In Figure 3b, the bandgap of MBI keeps decreasing under the effect of electric field and eventually is reduced to

be around 1.1 eV. This bandgap value is then maintained until the end of the simulation even in the absence of electric field. In addition, the shrinking of bandgap is the result of PDoS expansion of the Bi atoms and I atoms, rather than the generation of gap states. In addition, the applied electric field also significantly doped the MBI to an n-type material. As the Fermi level approaches the conduction band edge, the bulk conductivity of MBI increases significantly.

In addition to the simulation performed with electric field of 3 V nm^{-1}, the effect of a large electric field of 10 V nm^{-1} was also investigated. The evolution of bandgap has been summarized in Figure 3c. Intriguingly, contrary to the gradual decrease in the bandgap caused by the 3 V nm^{-1} electric field, under the 10 V nm^{-1} electric field, the bandgap quickly decreases to 0 within the simulation time of 0.8 ps. A video recording the AIMD

**ADVANCED
SCIENCE NEWS**

www.advancedsciencenews.com

**ADVANCED
INTELLIGENT
SYSTEMS**
Open Access

www.advintellsyst.com

simulation has been provided in Movie S2, Supporting Information. The video shows the abrupt collapse of the primitive cell structure of MBI, which may be caused by the ionization of material triggered by the high electric field. The results of the two simulations suggest that changing the phase structure and conductivity of the MBI material needs to overcome an energy barrier. Compared with the breakdown of the structure, the structural phase change of the MBI perovskite causes the conductivity to change.

Furthermore, through the evolution of electron charge density distribution, we tried to uncover a charge-exchange origin of the electronic structure change of MBI perovskite in the simulation. The electron density distributions of the MBI structures are plotted in Figure 3d. An example of the atomic structure and charge isosurface (0.05 e bohr^{-3}) was illustrated in 3D and from the critical moment of the atomic structure change, the 2D electron density distribution map was sampled using the red lattice plane shown in the 3D image. The sites of major charge exchange are highlighted using the dashed white circles. Without electric field bias, the structures of MBI do not show significant charge interaction between $Bi_2I_9^{3-}$ and MA^+, whereas the charge exchange is intensified due to the rotation of MA^+ driven by electric field. Moreover, the initiation and termination of strong electron exchange are matched with the period when the material bandgap decreases and electron doping concentration increases.

The presence of the iodine vacancy-induced defect states at the MBI NW/PAM interface was also thoroughly investigated to explore the possibility of such defects contributing to the device conductance modulation, as shown in Figure S7, Supporting Information. The MBI with defects at the interface of PAM exhibited DoS characteristics similar to the MBI without defects at the PAM interface along with the constant presence of the Fermi level in the middle of bandgap, thereby confirming the incapability of such defects in modulating device conductance. Therefore, the calculation results support that, through the rotation of MA^+ cluster, the charge exchange between $Bi_2I_9^{3-}$ and MA^+ is the origin of electronic structure change of MBI perovskite.

2.4. Artificial Synapses for Processing/learning Tasks

The MBI NW device was subjected to repeated cyclic $I–V$ sweeps (0 V → 3 V→ 0 V), as shown in **Figure 4**a. It can be observed that with increasing cycle number, the device conductance increases, demonstrating potentiating behavior. Also evident from the log-scale plot of the first cycle $I–V$ sweep in Figure S8a, Supporting Information and the successive linear sweeps in Figure 4a, the change in the device conductance is extremely gradual in nature without any steep jump in conductance, which is a necessity for neuromorphic processing devices.[34] Similar cyclical $I–V$ sweeps within the voltage range 0 V → 2 V→ 0 V, shown in Figure S8b, Supporting Information, demonstrate the potentiation capability of the device with lower current and hence lower power expenditure. The lower operating current is attributed to the weaker rotation of the MA^+ clusters triggering the conductance change and
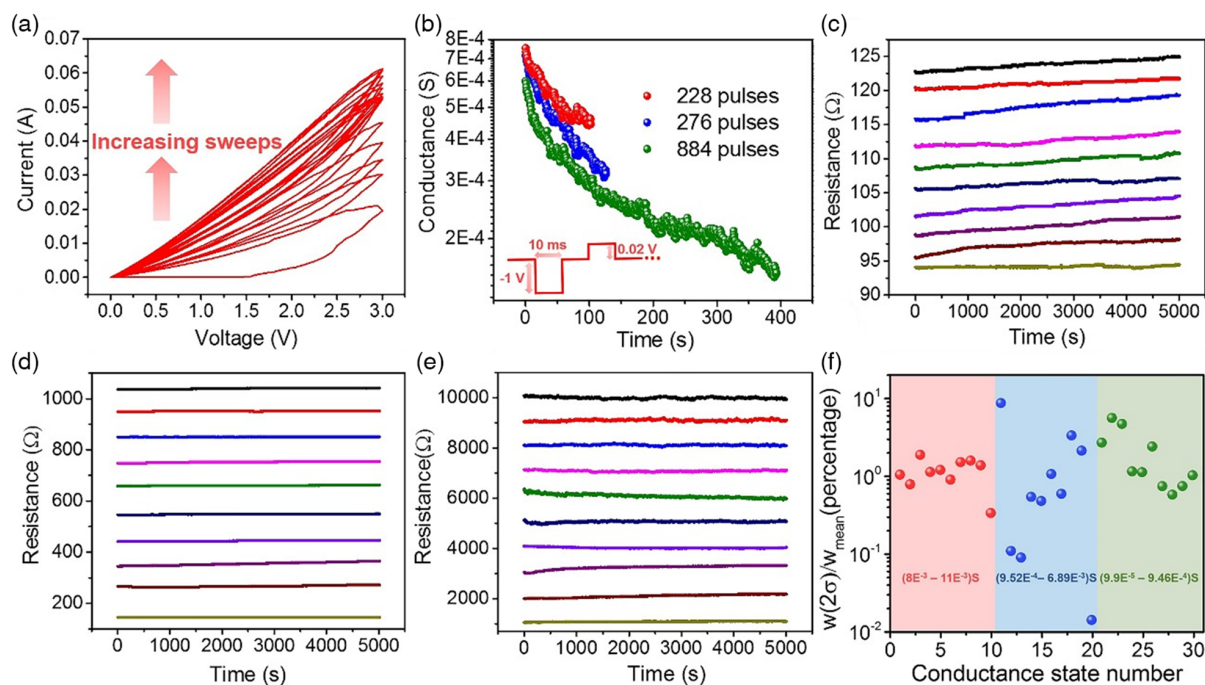
Figure 4. Paving the way for performing processing tasks with MBI NW artificial synapses. a) $I–V$ characteristics of MBI NW device exhibiting enhanced conductance upon increasing number of sweeps. b) Modulation of device conductance in MBI NW artificial synapse with varying number of depression pulses. c) Demonstration of 10 temporally stable LTP conductance states within the resistance range between ≈90 Ω and 125 Ω. d) Demonstration of 10 temporally stable LTP conductance states within the resistance range between ≈145 Ω and 1.05 kΩ. e) Demonstration of 10 temporally stable LTP conductance states within the resistance range between ≈1.057 kΩ and 10.1 kΩ. f) Temporal jitter or variation (2 × standard deviation (σ)/mean) of the LTP conductance states corresponding to (c)–(e).

ADVANCED
SCIENCE NEWS
www.advancedsciencenews.com

ADVANCED
INTELLIGENT
SYSTEMS
Open Access
www.advintellsyst.com

subsequently lesser charge exchange between the MA^+ and $Bi_2I_9{}^{3-}$ species. The negative cyclical I–V sweeps ($0\,V \rightarrow -3\,V \rightarrow 0\,V$) have also been provided in Figure S8c, Supporting Information, exhibiting the depression trend upon increased number of cycles.

To modulate the synaptic weights for performing processing tasks, it is needed that distinct and temporally stable conductance states of the artificial synaptic devices be accessed.[35] In the MBI NW device, the desired conductance state was obtained by applying trains of potentiation-depression pulses. Such an instance is shown in Figure 4b, wherein with different depression pulse ($-1\,V/0.02\,V$ amplitude and 10 ms width) numbers, the desired conductance state could be achieved within the conductance range from 10^{-4} to $10^{-3}\,S$ (from 1 to 10 kΩ resistance range). Similar attainment of desired conductance in the range from 10^{-3} to $10^{-2}\,S$ with input depression pulses has been shown in Figure S8d, Supporting Information. The more the number of accessed conductance states, better is the processing potential of the artificial synapses. 30 such conductance states within the resistance range from 90 Ω to 10.1 kΩ, read out with a read voltage of 0.01 V, have been shown in Figure 4c–e. Each of the 30 states demonstrated excellent electrical stability and low jitter with optimal variation ($2\sigma/\text{mean}$) <10%, as shown in Figure 4f. Detailed measurements of the retention time ability for the LTP conductance states were carried out, as shown in Figure S9, Supporting Information. As shown in Figure S9a, 10 states within the resistance range from 1 to 10 kΩ (different from the ones shown in Figure 4e) showed excellent retention capability without any degradation $>10^5\,s$ at a reading voltage of 0.01 V only. To further demonstrate the robustness of the LTP conductance states, we carried out intermittent retention measurements, shown in Figure S9b, Supporting Information, where instead of a continuous DC bias of 0.01 V, sporadic reading DC bias of 0.01 V was applied to the device after every 30 min for 2 h and the LTP states remained unaltered for the entire duration. Also, the total number of conductance states accessed now counts to 40, after adding the ones shown in Figure 4e and S9, Supporting Information. To the best of our knowledge, this is the longest retention time and highest number of accessed LTP states of perovskite-based artificial synapses known so far and is also at par with the traditional material systems reported previously. (For details see Table S1, Supporting Information that compares the various figures of merit of MBI NW artificial synapses with previously reported perovskite and NW based artificial synapses). We also performed a comparative study of the LTP conductance state's stability for TF MBI and NW-based MBI devices. The TF devices were observed to be more prone to LTP retention failure as compared with the NW devices. Two modes of failure were observed, as shown in Figure S10a,b, Supporting Information respectively. In some of the devices, the degradation of the LTP conductance state was gradual (Figure S10a, Supporting Information) and in some the change was rather abrupt (Figure S10b, Supporting Information). A statistical study on batches of 10 TF and 10 NW devices revealed that for a particular conductance state ($\approx 2.22 \times 10^{-4}\,S$ for instance, as shown in Figure S10c, Supporting Information), the NW LTP states remained intact for $10^5\,s$. The TF LTP states however showed a relatively high variation of retention time with a mean of 37 252 s. This performance improvement in MBI NW-based synapses compared with TF devices and also relative to previously

reported TF-based perovskite synapses is attributed to the excellent mechanical and electrical stability instilled by the PAM passivation. Specifically the PAM prevented external oxygen and water molecules to attack the environmentally delicate perovskite material, thereby improving material robustness and device lifetime.[17,32]

Device power consumption reduction strategies have been discussed in detail in Figure S11, Supporting Information. Specifically, the reduction in top electrode size to a $40\,\mu m \times 40\,\mu m$ square helped in drastically reducing the operating current to $\approx\mu A$ range. The device operational reliability was tested for a batch of 100 devices, exhibiting excellent distinguishability among the current states (see Figure S12a, Supporting Information). The devices could endure the I–V mode for $>10^4$ cycles and the pulse mode for $\approx 10^5$ cycles without any degradation in performance, as can be seen from Figure S12b,c, Supporting Information. It is worth mentioning that the PAM-induced excellent electrical stability rendered the MBI NW synapses to possess the highest endurance among reported perovskite artificial synapses, to the best of our knowledge.

2.5. Implementing Letter Recognition Emulating Gestalt Principle of Closure

As shown in **Figure 5**a, a single-layered ANN was successfully constructed to recognize five full letters, 'H,K,U,S,T', as well as their defected or fragmented letters. An illustration of all the fragmented letters has been provided in Figure S13, Supporting Information. Each letter, the training dataset, is a 6×3 binary image, which is either 1 or 0 for each pixel, as shown in Figure 5a. The structure of this neural network consists of 18 pixels input which represent the five letters and then the signal from the input is relayed to the memristor-based (MBI NW synapse array) neural network for processing and ultimately uses five letters as the neuronal output. The input, a 6×3 binary digit image with each pixel, is represented by a voltage equal to either 0.01 or 0 V, connecting to one synaptic cell. The input voltage is chosen to be 0.01 V for low power consumption achieved by MBI NW devices because such a small voltage is already enough to actuate the system. Each effective cell comprised one MBI NW device and one resistance with constant value ($\approx 1\,k\Omega$) such that there are totally 18 MBI NW devices and 18 fixed value resistances in one row corresponding to 18 pixels for each input letter. See Figure S14, Supporting Information for detailed input/output connections and the image of the device. We should notice that the data is processed in parallel as in our brain and the power consumption is only due to the current flowing through the MBI NW device. Thus, the data processing speed for big data is also potentially fast with ultralow power consumption. Then we obtain the output current as the differential value following Kirchhoff's law, $\sum_{i=1}^{18} I_{\text{mem}} - \sum_{i=1}^{18} I_{\text{res}}$, between the summed memristor current, $\sum_{i=1}^{18} I_{\text{mem}}$ and resistance current, $\sum_{i=1}^{18} I_{\text{res}}$. As shown in Figure 5a, the final letter neuronal output, l_n is calculated as the nonlinear activation function of output current as shown and the input image will be classified as the letter with largest letter neuronal output from each row.
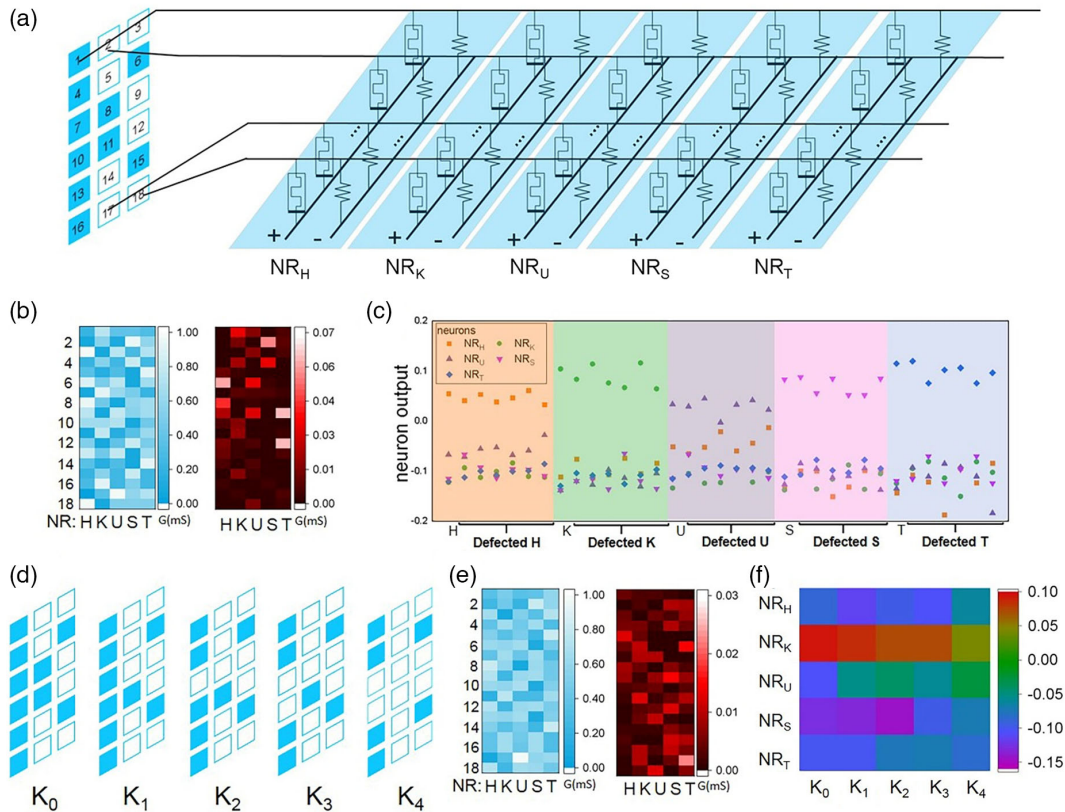
Figure 5. Implementing emulation of Gestalt principle of closure by letter recognition using MBI NW-based neural network. a) Single-layered neural network used for classifying the letters 'H,K,U,S,T' in their defected and complete form. b) Conductance distribution of the trained network within the range from 0.1 to 1 mS (left). Deviation between the simulation and empirical conductance values for the single-layered neural network (right). c) Graphical illustration of neuronal outputs corresponding to the complete and defected letters exemplifying Gestalt closure recognition task. d) Illustration showing 1 complete letter K and four defected Ks. e) Conductance distribution (left) and deviation between simulated and empirical conductance values of network used to complete recognition task corresponding to (d). f) Neuronal output map exhibiting the difficulty in letter recognition with increasing missing fragments of a letter.

$$l_{n} = \tanh\left(\beta\left(\sum_{i=1}^{18} I_{mem} - \sum_{i=1}^{18} I_{res}\right)\right) \quad (1)$$

where n represents H, K, U, S, or T and β is a constant <1, used to adjust the synaptic weights.

We established the MBI NW device-based letter recognition depending on the Delta rule in off-line training mode.[6,36] We trained the single-layered ANN with the help of software first and then transferred the weights into the conductance of the MBI NW devices (refer to supporting information for more details). We applied positive pulse (potentiation) to increase the conductance while negative pulse (depression) to decrease the conductance and finally achieved the accurate conductance value of memristor. For example to achieve 1 kΩ resistance or 1 mS conductance as the synaptic weight, 200 potentiation pulses are fed to the device. However, the resistance/conductance level might have been 1.2 kΩ or 0.83 mS after the application of the pulse train. To bring the weight to its desired value, then we applied 20 depression pulses to ensure as much accuracy as possible in the off-chip training. In Figure 5b,c, we realized the recognition of five full letters and their fragmented counterpart. The

broken letter is formed by setting one line of the complete letters as null. As each letter has six rows, there are totally six defected letters for each complete letter. Thus, for each letter, there are totally 7 points (the first point representing the complete letter and the next six representing the defected ones) which are marked by different colors in Figure 5c. Figure 5b shows the conductance distribution of the well-trained network, from 0.1 to 1 mS of MBI NW synapses, and the deviation compared with simulation value has been shown in the right. The minor deviation arose from conductance drift during testing and could not hinder the recognition task. As shown in Figure 5c, the neuronal outputs of each full letter and six defected letters, along γ-axis, were calculated. The MBI NW-based letter recognition model achieved 100% accuracy as each letter neuron showed the largest response to corresponding letter. If we check the letter neuron output carefully, we will notice that the value for third defected 'U' is close to the letter neuron 'H'. It is because the defected letter 'H' with third line missing and the defected image 'U' with sixth line missing resemble each other very closely.

Subsequently, to verify the generalization ability of MBI NW ANN, we only involved full letters as training data and checked the letter neuron outputs of defected letters. As illustrated in

Figure 5d, there is one full letter 'K' and four defected 'K's with more pixels missing from left to right, which increase the degree of difficulty for recognizing the input image. In Figure 5e, we have shown the conductance distribution and deviation of this memristor-based network. Next, we utilized the trained MBI NW-based neural network for classification of both full letter and defected letters. As we can see in Figure 5f, the letter neuron output 'K' is in the second row and with more pixels missing, the response strength of letter neuron, 'K', diminishes while the signal of other letter neurons becomes a little bit stronger. It fits the narrative of the Gestalt principle of closure as both human visual perception and MBI NW-based neuron network prefer a relatively complete shape. However, the defected image will make the classification harder but will never completely confuse the classification results and will only decrease the probability of certain labels. The successful letter recognition demonstration using our perovskite memristor device proves the effectiveness of MBI NW artificial synapses-based ANN for performing neuromorphic processing tasks emulating human cognitive traits.

3. Conclusion

In summary, we demonstrated a letter recognition scheme mimicking the cognitive learning model of Gestalt principle of closure with MBI perovskite NW array-based artificial synapses. The devices exhibited STP and LTP modes of learning with gradual transformation from STP to LTP with increasing number of stimulating voltage pulses. To explore the origin of intrinsic conductance change in monocrystalline MBI perovskite, we carried out initiatory AIMD simulations which revealed that it is the rotation of MA^+ clusters under electric field that triggers the charge exchange between MA^+ and $Bi_2I_9^{3-}$, causing the gradual conductivity modulation. 40 LTP conductance states with excellent retention of $>10^5$ s and minimum variation $<10\%$ paved the way for building the MBI NW synapse-based artificial neural network to implement the Gestalt principle of closure. The network thus formed achieved recognition task of 5 distinct fragmented letters as it did for the complete version of the same 5 letters. Also the network showed that much like the human brain, MBI NW synaptic array could also distinguish one defected letter more easily with lesser number of missing parts. All in all, this work uplifts halide perovskite to be used in complex neuromorphic processing tasks and opens up a new vista of exploring pattern recognition emulating human cognition with memristor-based ANNs, ultimately paving the way for alleviation of brittleness associated with conventional AI systems by incorporating abstraction and common sense comprehension.

4. Experimental Section

Materials: Methyl Ammonium Iodide (MAI) powder was purchased from DYESOL.

Device Fabrication: 1.5 cm × 2 cm Al chips were electropolished to remove the surface roughness. A highly ordered porous alumina membrane or PAM was obtained post a two-step anodization process using 0.2 M oxalic acid at 40 V. The PAM was then barrier thinned by a voltage ramping down process and subsequently metallic bismuth (Bi) was electrodeposited in the channels to facilitate growth of the MBI NWs. Following a VSSR process between methyl ammonium iodide (MAI) powder and electrodeposited Bi at 180 °C and 300 sccm continuous Ar flow, the highly ordered MBI NWs were obtained within the confines of the PAM walls. This process of perovskite NW growth was reported by us recently.[37,38] ITO electrodes of area 7.06 mm^2 were deposited as the top electrode via a radio frequency (RF) sputtering process using a power of 200 W and pressure of ≈0.23 Pa. Finally, NOA81 UV-curable epoxy was used to package the devices.

TEM and FIB Characterization: The fabrication of the lamella for transmission electron microscopy (TEM) imaging was carried out using dual-beam focused ion beam (FIB)/FESEM system, FEI Helios G4 UX, containing both focused Ga^+-ion beam and an ultrahigh-resolution field-emission scanning electron column that can be used in synchrony. The imaging and EDS study of the NWs were done using a transmission electron microscope JEM 2010 (JEOL).

AIMD Simulation: The AIMD simulation was performed using the Car–Parrinello molecular dynamics code integrated in Quantum Espresso.[39,40] The simulation was performed using the NVT ensemble. NVT ensemble refers to a group of systems whose thermodynamic state is dictated by a fixed number of atoms (N), a fixed volume (V) and a fixed temperature (T). The primitive cell structure of $MA_3Bi_2I_9$ was first relaxed for 2000 steps to reach a steady position. Then, a homogeneous finite electric field described through the modern theory of the polarization was applied along the z-axis. The self-consistency calculation was implemented with the Perdue–Burke–Ernzerhof exchange-correlation functional and ultrasoft pseudopotential was used to treat the core electrons for all the atomic species. The convergence threshold for the self-consistency calculation was set to 10^{-6} Ry and the Verlet algorithm was used to update the atomic structure and electronic structure. The atom-PDoS and the electron charge density calculation were calculated in first principles using the Quantum Espresso. To perform the self-consistency calculation, the core electrons were treated with the ultrasoft pseudopotential and the Perdue–Burke–Ernzerhof functional was utilized as the exchange correlation functional. The k-space grid sampling was generated using the $4 \times 4 \times 4$ Monkhorst-Pack scheme and the electron convergence threshold was set to 10^{-6} Ry.

Electrical Characterization: The artificial synaptic characterization of the MBI NW devices, involving generation of electrical pulses of varying amplitude, width, interval, and subsequent recording of output current, was carried out using the arbitrary waveform generator module of the Keithley 4225 PMU and Keithley 4200 SCS systems. The tuning and recording of the temporally stable LTP conductance levels and I–V characterization were done with Keithley 2450 source meter and home-built LABVIEW programs. The off-chip training of the single-layered MBI NW-based neural network and reading out the requisite output synaptic currents was performed with the Keithley 2450 source meter, home-built and assembled systems including LABVIEW programs, National Instruments controller, multiplexer, and source meter.

Supporting Information

Supporting Information is available from the Wiley Online Library or from the author.

Acknowledgements

Conflict of Interest

The authors declare no conflict of interest.

Author Contributions

Z.F. and S.P.: conceptualized the experiments and analyzed the results. S.P.: carried out the device fabrication and detailed structural and electrical characterizations including TEM study, artificial synaptic characterization, resistance state tuning, and Gestalt learning model implementation. Z.C.: performed the neural network simulations. Z.M.: performed the molecular dynamics simulation to decipher the conductance modulation in MBI perovskite. Y.Z.: helped with the resistance state tuning and device fabrication. C.L.J.C.: helped with the implementation of the Gestalt Learning neural network. B.R., Q.Z., D.Z., G.S., and H.Z.: helped with device fabrication and characterization. All authors participated in manuscript writing and articulation.

Data Availability Statement

The data that support the findings of this study are available from the corresponding author upon reasonable request.

Keywords

artificial synapses, Gestalt principle of closure, letter recognition, perovskite nanowires

[1] M. Wertheimer, *Gestalt Theory*, **1938**.
[2] W. Köhler, *Psychol. Forsch.* **1967**, *31*, XVIII.
[3] K. Koffka, *Principles of Gestalt Psychology*, Routledge, London, UK **2013**.
[4] S. Coren, J. S. Girgus, *J. Exp. Psychol. Hum. Percept. Perform.* **1980**, *6*, 404.
[5] P. Yao, H. Wu, B. Gao, S. B. Eryilmaz, X. Huang, W. Zhang, Q. Zhang, N. Deng, L. Shi, H.-S. P. Wong, *Nat. Commun.* **2017**, *8*, 1.
[6] M. Prezioso, F. Merrikh-Bayat, B. Hoskins, G. C. Adam, K. K. Likharev, D. B. Strukov, *Nature* **2015**, *521*, 61.
[7] G. Wu, H. Ji, *Soft Comput.* **2022**, 1.
[8] S. Yu, B. Gao, Z. Fang, H. Yu, J. Kang, H. S. P. Wong, *Front. Neurosci.* **2013**, *7*, 186.
[9] R. I. Damper, S. R. Harnad, *Percept. Psychophys.* **2000**, *62*, 843.
[10] H. Sano, B. K. Jenkins, *Comput. Music J.* **1989**, *13*, 41.
[11] W. Lotter, G. Kreiman, D. Cox, *Nat. Mach. Intell.* **2020**, *2*, 210.
[12] Y. Wang, Z. Lv, J. Chen, Z. Wang, Y. Zhou, L. Zhou, X. Chen, S. T. Han, *Adv. Mater.* **2018**, *30*, 1802883.
[13] H. Tian, L. Zhao, X. Wang, Y.-W. Yeh, N. Yao, B. P. Rand, T.-L. Ren, *ACS Nano* **2017**, *11*, 12247.
[14] S. Chen, J. Huang, *ACS Appl. Electron. Mater.* **2020**, *2*, 1815.
[15] Q. Zhang, D. Zhang, L. Gu, K.-H. Tsui, S. Poddar, Y. Fu, L. Shu, Z. Fan, *ACS Nano* **2020**, *14*, 1577.
[16] D. Zhang, L. Gu, Q. Zhang, Y. Lin, D.-H. Lien, M. Kam, S. Poddar, E. C. Garnett, A. Javey, Z. Fan, *Nano Lett.* **2019**, *19*, 2850.
[17] A. Waleed, M. M. Tavakoli, L. Gu, S. Hussain, D. Zhang, S. Poddar, Z. Wang, R. Zhang, Z. Fan, *Nano Lett.* **2017**, *17*, 4951.
[18] L. Gu, D. Zhang, M. Kam, Q. Zhang, S. Poddar, Y. Fu, X. Mo, Z. Fan, *Nanoscale* **2018**, *10*, 15164.
[19] M. Lyu, J. H. Yun, P. Chen, M. Hao, L. Wang, *Adv. Energy Mater.* **2017**, *7*, 1602512.
[20] G. Milano, M. Luebben, Z. Ma, R. Dunin-Borkowski, L. Boarino, C. F. Pirri, R. Waser, C. Ricciardi, I. Valov, *Nat. Commun.*, **2018**, *9*, 1.
[21] C. Shen, X. Gao, C. Chen, S. Ren, J. L. Xu, Y. D. Xia, S. D. Wang, *Nanotechnology* **2021**, *33*, 065205.
[22] Y. Meng, F. Li, C. Lan, X. Bu, X. Kang, R. Wei, S. Yip, D. Li, F. Wang, T. Takahashi, T. Hosomi, *Sci. Adv.* **2020**, *6*, eabc6389.
[23] Y. Yu, C. Wang, C. Jiang, L. Wang, Z. Wang, Z. Du, J. Sun, I. Abrahams, X. Huang, *J. Alloys Compd.* **2021**, *868*, 159194.
[24] H. Wang, J. Tian, K. Jiang, Y. Zhang, H. Fan, J. Huang, L.-M. Yang, B. Guan, Y. Song, *RSC Adv.* **2017**, *7*, 43826.
[25] J. K. Pious, M. Lekshmi, C. Muthu, R. Rakhi, V. C. Nair, *ACS Omega* **2017**, *2*, 5798.
[26] S. Poddar, Y. Zhang, Y. Zhu, Q. Zhang, Z. Fan, *Nanoscale* **2021**, *13*, 6184.
[27] G. Sun, A. G. Kirk, *Opt. Express* **2007**, *15*, 13149.
[28] T. Ohno, T. Hasegawa, T. Tsuruoka, K. Terabe, J. K. Gimzewski, M. Aono, *Nat. Mater.* **2011**, *10*, 591.
[29] Z. Wang, S. Joshi, S. E. Savel'ev, H. Jiang, R. Midya, P. Lin, M. Hu, N. Ge, J. P. Strachan, Z. Li, *Nat. Mater.* **2017**, *16*, 101.
[30] S. Choi, S. H. Tan, Z. Li, Y. Kim, C. Choi, P.-Y. Chen, H. Yeon, S. Yu, J. Kim, *Nat. Mater.* **2018**, *17*, 335.
[31] F. Ma, Y. Zhu, Z. Xu, Y. Liu, X. Zheng, S. Ju, Q. Li, Z. Ni, H. Hu, Y. Chai, *Adv. Funct. Mater.* **2020**, *30*, 1908901.
[32] B. Wang, K. Y. Wong, S. Yang, T. Chen, *J. Mater. Chem. A* **2016**, *4*, 3806.
[33] E. J. Juarez-Perez, L. K. Ono, M. Maeda, Y. Jiang, Z. Hawash, Y. Qi, *J. Mater. Chem. A* **2018**, *6*, 9604.
[34] H. Yeon, P. Lin, C. Choi, S. H. Tan, Y. Park, D. Lee, J. Lee, F. Xu, B. Gao, H. Wu, *Nat. Nanotechnol.* **2020**, *15*, 574.
[35] J. Tang, C. He, J. Tang, K. Yue, Q. Zhang, Y. Liu, Q. Wang, S. Wang, N. Li, C. Shen, *Adv. Funct. Mater.* **2021**, *31*, 2011083.
[36] E. Zamanidoost, F. M. Bayat, D. Strukov, I. Kataeva, presented at *2015 IEEE 9th Int. Symp. on Intelligent Signal Processing (WISP) Proc.*, IEEE, Piscataway, NJ **2015**.
[37] A. Waleed, M. M. Tavakoli, L. Gu, Z. Wang, D. Zhang, A. Manikandan, Q. Zhang, R. Zhang, Y.-L. Chueh, Z. Fan, *Nano Lett.* **2017**, *17*, 523.
[38] L. Gu, M. M. Tavakoli, D. Zhang, Q. Zhang, A. Waleed, Y. Xiao, K. H. Tsui, Y. Lin, L. Liao, J. Wang, *Adv. Mater.* **2016**, *28*, 9713.
[39] P. Giannozzi, O. Andreussi, T. Brumme, O. Bunau, M. B. Nardelli, M. Calandra, R. Car, C. Cavazzoni, D. Ceresoli, M. Cococcioni, *J. Condens. Matter Phys.* **2017**, *29*, 465901.
[40] P. Giannozzi, S. Baroni, N. Bonini, M. Calandra, R. Car, C. Cavazzoni, D. Ceresoli, G. L. Chiarotti, M. Cococcioni, I. Dabo, *J. Condens. Matter Phys.* **2009**, *21*, 39550.